Synthesis of Pd_9Ru@Pt nanoparticles for oxygen reduction reaction in acidic electrolytes

Yu Sun[a], Yu-Chi Hsieh[b], Li-Chung Chang[a], Pu-Wei Wu[c,*]

Jyh-Fu Lee[d]

[a]Graduate Program for Science and Technology of Accelerator Light Source

National Chiao Tung University, Hsin-chu 300, Taiwan, ROC

[b]Brookhaven National Laboratory, Chemistry Department

Building 555, Upton, NY 11973, USA

[c]Department of Materials Science and Engineering,

National Chiao Tung University, Hsin-chu 300, Taiwan, ROC

[d]National Synchrotron Radiation Research Center, Hsin-chu 300, Taiwan, ROC

Abstract

Nanoparticles of PdRu, Pd_3Ru, and Pd_9Ru are synthesized and impregnated on carbon black via a wet chemical reflux process. X-ray diffraction patterns of the as-synthesized samples, Pd_xRu/C (x=1/3/9), suggest succesful formation of alloy without presence of individual Pd and Ru nanoparticles. Images from transmission electron microscope confirm irregularly-shaped nanoparticles with average size below

3 nm. Analysis from extended X-ray absorption fine structure on both Pd and Ru K-edge absorption profiles indicate the Ru atoms are enriched on the surface of Pd_xRu/C. Among these samples, the Pd_9Ru/C exhibits the strongest electrocatalytic activity for oxygen reduction reaction (ORR) in an oxygen-saturated 0.1 M aqueous $HClO_4$ solution. Subsequently, the Pd_9Ru/C undegoes Cu under potential deposition, followed by a galvanic displacement reaction to deposit a Pt monolayer on the Pd_9Ru surface ($Pd_9Ru@Pt$). The $Pd_9Ru@Pt$ reveals better ORR performance than that of Pt, reaching a mass activity of 0.38 mA μg^{-1}_{Pt}, as compared to that of commercially available Pt nanoparticles (0.107 mA μg^{-1}_{Pt}). The mechanisms responsible for the ORR enhancement are attributed to the combined effects of lattice strain and ligand interaction. In addition, this core-shell $Pd_9Ru@Pt$ electrocatalyst represents a substantial reduction in the amount of Pt consumption and raw material cost.

Keywords: Palladium; Ruthenium; Platinum; Oxygen reduction reaction; Core-shell nanoparticles

* Corresponding author. Tel.: +886 3 5131227; fax: +886 3 5724727.

E-mail address: ppwu@mail.nctu.edu.tw (P.-W. Wu).

1. Introduction

Energy crisis has been a challenging issue all over the world for years. To moderate the carbon dioxide emission and the usage of fossil fuels, the development of affordable and environmentally friendly energy sources is extremely important. Among many alternative energy sources, the proton exchange membrane fuel cell (PEMFC) is considered as a promising candidate for its notable advantages including high power density and low operating temperature [1-4]. The operation of PEMFC involves a coupled reduction and oxidation of hydrogen and oxygen in an acidic electrolyte to produce electricity with the byproduct of water. It is recognized that the oxygen reduction reaction (ORR) at the cathode is the rate-limiting step because the dissociation of oxygen molecules is intrinsically sluggish [5-7]. Hence, it is important to identify suitable electrocatalysts for ORR actions. To date, Pt is the predominant choice for its chemical stability, and the Pt has been synthesized in different morphologies and nanostructures with varying degrees of ORR activities [8, 9].

Since Pt is a noble metal known for many industrial applications, it is desirable to minimize the Pt consumption in order to reduce the overall PEMFC system cost for commercial viability [10, 11]. A widely-employed strategy is the formation of alloyed nanoparticles. For example, binary electrocatalysts including Pt-Fe, Pt-Co, Pt-Cu, and Pt-Ni, as well as ternary electrocatalysts such as Pt-V-Co and Pt-Fe-Co have been

studied with various success [12-19]. Among them, the Pt_3Ni demonstrates very impressive activity and stability, with an ORR activity about 90 times larger than that of pure Pt [17].

Another approach to reduce the Pt consumption is the fabrication of core-shell (core@shell) nanostructured electrocatalysts [20-24]. This would also lead to considerable improvement in the catalytic activity due to strain and ligand effects. For example, Mani et al. and Wang et al. have prepared Pd@Pt and dealloyed Cu@Pt for improved ORR performances and they identified factors such as the altered electronic structure and reconstructed lattice that facilitate surface adsorption via a reduced free-energy barrier [20, 21]. To achieve desirable core@shell configuration, a variety of fabrication schemes including electrochemical dealloying, chemical leaching, absorbate-induced segregation, thermally-induced segregation, and galvanic displacement, have been explored [25-35]. Among them, the deposition of mono-layered Cu, known as Cu under potential deposition (Cu upd), followed by a galvanic displacement reaction to replace the Cu by Pt, has opened many possibilities for inexpensive cores with surface coated by a monolayered Pt [32-36]. The improved ORR activities from such Pt-monolayered electrocatalysts are attributed to both strain (geometric effect) and electronic interaction between the monolayered Pt atoms and the core material (ligand effect) [37-39].

To date, Pt-monolayer deposited on Pd nanoparticles has attracted considerable attention because the Pd atoms underneath produce a slight compression of the Pt atoms on the surface. This engenders a reduction the *d*-band center in the Pt atoms that is conductive to ORR action [40]. Recently, in order to further weaken the binding energy of oxygen molecules on the surface Pt atoms for enhanced ORR, the Pd is alloyed with other elements. For example, systems including Pd-Ir, Pd-Au, Pd-Cu, Pd-Co, and Pd-Au-Ni have been employed as the core materials for monolayered Pt deposition and evaluated for ORR activities [23, 32-35].

Earlier, a theoretical study published by Zhang et al. on monolayered $Pt_{0.8}M_{0.2}$ (M=Ir/Ru/Rh/Pd/Au/Re/Os) deposited on a single crystalline Pd (111) surface had estimated the interaction energy between the $Pt_{0.8}M_{0.2}$ surface and two OHs, or OH and O in a (2×2) unit cell. Since the Ru is known to have a relatively high coverage of OH at a lower potential than that of Pt, a stronger ORR activity was predicted for the $Pt_{0.8}Ru_{0.2}$/Pd (111) configuration [41]. Because the single crystalline Pd (111) surface is not a practical substrate for PEMFC, it would be more appropriate to fabricate PdRu nanoparticles whose surface was enriched with the Ru atoms, and attempt to have monolayered Pt deposition on the PdRu surface. Previously, the synthesis of PdRu nanoparticles have been explored in the electro-oxidation of methanol, ethanol, and formic acid in alkaline [42] and acidic electrolytes [43, 44]. To

the best of our knowledge, the adoption of PdRu as a substrate to support monolayered Pt for ORR action in an acidic electrolyte has not been reported yet. In this work, we demonstrate the synthesis of Pd_xRu (x=1/3/9) nanoparticles and evaluate their ORR activities. We find that the Pd_9Ru reveals the strongest ORR behavior and use the Pd_9Ru as the core to support monolayered Pt for better ORR performance than those of Pd and Pd@Pt.

Experimental

2.1 Synthesis of Pd_xRu/C (x=1/3/9) nanoparticles

Carbon-supported Pd_xRu (x=1/3/9) nanoparticles were synthesized by a chemical reduction route. First, 80 mg of carbon black (Vulcan XC-72R) was suspended in 50 mL of deionized water by sonication. Next, appropriate amounts of $PdCl_2$ (Echo Chemical Inc., Palladium content 59.8 wt%) and $RuCl_3\,nH_2O$ (Sigma-Aldrich, ruthenium content 40 wt%) were dissolved in 50 mL of deionized water (molar ratio of Pd/Ru=1, 3, 9), and later mixed with the XC72R suspension. Afterward, 50 mg of sodium citrate dihydrate (J.T. Baker, ≧99 wt%) was added as a chelating agent and minute amount of 0.5 M NaOH was added to adjust the pH of the mixture to 12. At this stage, 20-fold mole of $NaBH_4$ (Sigma-Aldrich, ≧98.5 wt%) was added as a reducing agent. The mixture underwent stirring for 2 h at 80˚C in an argon flow under

reflux to obtain a homogeneous ink dispersion. Then, the Pd_xRu nanoparticles were filtered and thoroughly washed to remove residual chloride ions. These as-synthesized carbon-supported Pd_xRu nanoparticles, denoted as Pd_xRu/C, were dried at 25˚C in air, followed by a reduction treatment at 80˚C for 2 h in 5% H_2 and 95% Ar. The effective metal loading of the Pd_xRu/C catalysts were kept at 20 wt%.

2.2 Formation of Pd_9Ru@Pt/C nanoparticles

To prepare the Pd_9Ru@Pt/C nanoparticles, 5 mg of Pd_9Ru/C, 1.5 mL of isopropyl alcohol, 1 mL of deionized water, and 1 μL of 5 wt% Nafion ionomer dispersion (Sigma-Alrich) were properly mixed by sonication to render a homogeneous ink dispersion. Next, 15 μL of the ink dispersion was dropped onto a glassy carbon rotating disk electrode (RDE) serving as a working electrode (Pine Research, electrode diameter is 5 mm and the electrode area is 0.196 cm^2). Afterward, the working electrode was immersed in a deaerated aqueous solution containing 50 mM of $CuSO_4$ (Sigma-Aldrich) and 50 mM of H_2SO_4 (SHOWA) where 20 cyclic voltammetry (CV) scans with a scan rate of 20 mV s^{-1} in a potential window of 0.314 and 0.764 V (vs. RHE) were imposed. The purposes for these CV scans were to clean the surface of the Pd_9Ru/C, and identify the appropriate potential for Cu upd process. Subsequently, the Cu upd was carried out in a potential window of 0.314 and 0.764 V (vs. RHE) to form a monolayered Cu covering the surface of Pd_9Ru nanoparticles.

After the Cu upd treatment, the sample was removed from the plating solution and immersed in a deaerated aqueous electrolyte containing 1 mM K_2PtCl_4 and 50 mM H_2SO_4. At this stage, a displacement reaction was occurring in which the Cu atoms were oxidized whereas the Pt ions from the electrolyte were reduced to form a Pt monolayer on the surface of Pd_9Ru. The sample, undergoing the entire Cu upd and displacement reaction process, was label as Pd_9Ru@Pt/C.

2.3 Electrochemical analysis

ORR activities of the samples were measured in 0.1 M aqueous $HClO_4$ solution using a custom-made three electrode cell. The tests were conducted at 25˚C using a VersaSTAT electrochemical interface. The Ag/AgCl and Pt foil (15 cm^2) were used as the reference and counter electrode, respectively. The electrolyte was saturated with O_2 for 40 min prior to the experiments, and a CV scan between 0.824 and -0.226 V (vs. Ag/AgCl) was conducted at a scan rate of 10 mV s^{-1}. The potential for the reversible hydrogen electrode (RHE) was -0.276 V (vs. Ag/AgCl). In our figures, the potentials were plotted against the RHE. Identical electrochemical tests were performed on commercially available Pt/C (20 wt% Pt on XC72R, BASF) for comparison purpose.

2.4 Materials characterization

The morphology and size of the as-synthesized Pd_xRu nanoparticles were

obtained from a transmission electron microscope (Joel ARM 200F). X-ray diffraction (XRD) patterns for the as-synthesized Pd_xRu/C were obtained by a Bruker D2 Phaser equipped with a Cu Kα radiation source (λ= 1.54 Å) to identify relevant phases and particle sizes. Catalyst loadings of Pd_xRu/C and $Pd_9Ru@Pt/C$ were obtained by an inductively couple plasma mass spectrometry (ICP-MS; Agilent 7500ce). The X-ray absorption spectroscopy (XAS) experiments on the Pd K-edge (24,350 eV) and Ru K-edge (22,117 eV) were performed at BL01C1 and BL17C1 of the Taiwan Light Source (TLS), National Synchrotron Radiation Research Center (NSRRC), Hsin-chu, Taiwan. The detection was carried out in a fluorescence mode at 25˚C. Reference materials including Pd, $PdCl_2$, Ru, and RuO_2 were used. Extended X-ray absorption fine structure (EXAFS) data analysis and fitting were obtained by IFEFFIT 1.2.11c data analysis package (Athena, Artemis, and FEFF6). The raw data were calibrated by aligning the scans against the reference and merging multiple scans as an average to achieve better signal quality. X-ray absorption near edge structure (XANES) spectra were received after normalization by Athena software. The EXAFS function was obtained by standard procedures with Athena including pre-edge and post-edge subtraction, and normalization with respect to the edge jump. Details in the XAS measurements can be found elsewhere [45]. Relevant structural parameters such as the coordination number (N), bond distance (R), Debye-Waller factor ($\Delta\sigma_j^2$), and inner

potential shift (ΔE_0), were fitted by Artemis with theoretical standards generated by FEFF6 code.

3. Results and discussion

Fig. 1 displays the representative TEM images of PdRu/C, Pd_3Ru/C, and Pd_9Ru/C, respectively. These TEM images revealed uniform distributions of nanoparticles on the XC72R surface with moderate agglomeration. The average sizes, determined by measuring 100 randomly-selected nanoparticles in the TEM images, were 2.8 ± 0.9, 2.65 ± 0.76, and 2.63 ± 0.74 nm for PdRu/C, Pd_3Ru/C, and Pd_9Ru/C, respectively.

Fig. 2 demonstrates the XRD diffraction patterns of PdRu/C, Pd_3Ru/C, and Pd_9Ru/C, along with standard profiles of Pd (JCPDS: no. 88-2335) and Ru (JCPDS: no. 06-0663). According to the JCPDS data, the Pd exists in a fcc phase with (111), (200), and (220) diffraction signals located at 40.12°, 46.66°, and 68.13°, respectively. In contrast, the Ru adopts a hcp phase with the strongest peaks located at 38.38°, 42.18°, and 44.02°, respectively. Among our samples, the diffraction patterns exhibited typical peak-broadening phenomenon owing to the finite nanoparticle size. For both Pd_9Ru/C and Pd_3Ru/C, there appeared two notable diffraction peaks which were consistent with those of (111) and (200) peaks from a fcc Pd lattice. Without the presence of hcp Ru signals, we concluded that the Ru atoms were alloyed successfully

with the Pd matrix forming a fcc phase. In contrast, the diffraction pattern from the PdRu/C revealed a single broad peak around 40°, which was indicative of the merger of (111) and (200) peaks from the Pd lattice, as well as the (101) peak from the Ru lattice. According to the binary phase diagram of Pd and Ru, the Pd and Ru form an alloy in limited composition range where less than 5 at% Ru is able to dissolve in the Pd lattice [46]. Therefore, in the case of PdRu/C, it is possible that moderate Ru segregation took place in the nanoparticle but the likelihood of individual Ru nanoparticles was negligible due to the lack of distinguishable Ru (101) diffraction signal.

Since the atomic radius of Ru (1.34 Å) is relatively smaller than that of Pd (1.37 Å), the incorporation of the Ru atoms in the Pd lattice is expected to reduce the lattice parameter accordingly, and thus engenders a slight shift of the diffraction signals to higher anglers. From the position of the (220) diffraction angle, the lattice constant of PdRu/C, Pd_3Ru/C, and Pd_9Ru/C was determined as 3.874, 3.877, and 3.884 Å, respectively. In addition, the size of the nanoparticle estimated from the Scherrer's equation using the (220) diffraction peak was 3.9, 3.1, and 2.8 nm for PdRu/C, Pd_3Ru/C, and Pd_9Ru/C, respectively. The amount of Pd and Ru in the as-synthesized samples was determined by ICP-MS, and the ratio of Pd/Ru was consistent with our targeted composition.

The atomic distribution of Pd and Ru in the Pd_xRu nanoparticles can be obtained qualitatively by XAS spectra of Pd and Ru, respectively. Fig. 3 presents the Ru K-edge XANES profiles for PdRu/C, Pd_3Ru/C, and Pd_9Ru/C, as well as reference materials of Ru and RuO_2. In general, a sample with a lower occupancy of electronic states indicates a higher oxidation number, which gives rise to a greater white line intensity and a shift of absorption peak to higher energy. As expected, the spectra of Ru and RuO_2 revealed absorption energy at 22,117 and 22,121eV, respectively. The XAS profiles among our samples were rather consistent and their absorption energy were located around 22,118 eV, a value between Ru and RuO_2. We rationalized that the Ru atoms were prone to form surface oxide and hydroxide when they were in contact with electrolyte and therefore, the presence of Ru in a slightly oxidized state is anticipated [47].

The EXAFS profile is useful to determine the nature of neighboring atoms and the corresponding bonding distance, as well as the coordination number. Fig. 4 displays the Fourier-transformed EXAFS spectra of Ru K-edge along with the fitting results. Relevant parameters used in the fitting are provided in Table 1. As listed, the Ru formed separate bonding in Ru-O, Ru-Ru, and Ru-Pd, and the predominant bonding was Ru-Ru. In addition, the total coordination number, the sum of bonding arising from Ru-O, Ru-Ru, and Ru-Pd, was 6.41, 6.65, and 6.3 for PdRu/C, Pd_3Ru/C,

and Pd_9Ru/C, respectively. In the literatures, it is established that a smaller total coordination number suggests either a smaller nanoparticle size or the absorbing atom is simply residing on the surface. Due to the formation of Ru-O and the limited number of Ru-Pd bonding, we rationalized that in the Pd_xRu nanoparticles, the Ru atoms were enriched on the surface regime whereas the Pd atoms were mostly located at the core. This pattern agrees well with the XRD results that excludes the presence of Ru nanoparticles.

The profiles of XANES from Pd K-edge are demonstrated in Fig. 5. Interestingly, the absorption energy and the white line intensities of our samples were rather consistent and close to that of Pd. This further confirmed that in our samples, the Pd atoms mostly occupy the core with minimum interaction with the Ru atoms on the perimeter.

Fig. 6 presents the Fourier-transformed EXAFS spectra of Pd K-edge along with the fitting results. Relevant parameters used in the fitting are provided in Table 2. The Pd formed bonding in Pd-Pd and Pd-Ru, with a total coordination of 8.1, 9, and 8.6 for PdRu/C, Pd_3Ru/C, and Pd_9Ru/C, respectively. These numbers were consistently larger than those of Ru as listed in Table 1. This pattern supports our conclusion as atoms that reside predominately on the surface are expected to have fewer total bonding neighbors because of terminated coordination on the surface. It is noted that

in the fitting of XAS data, independent analysis of the EXAFS spectra from two components of the same catalyst in either alloyed or segregated state do not necessarily lead to a consistent result [48-50]. In order to reach a consistent result, in the Pd_xRu cases, the necessary conditions are *i*) both Pd and Ru atoms should be in reduced state and *ii*) the atomic ratio of Pd/Ru should be 1. The samples we synthesized are Pd_xRu (x=1/3/9), and the Ru atoms are enriched on the surface but exist in a slightly oxidized state. Therefore, it is reasonable that the coordination number of Ru-Pd is different from that of Pd-Ru.

The formation of Pd_xRu nanoparticles with surface-enriched Ru atoms can be validated by CV measurements in an acidic electrolyte. It is because the Ru is a known pseudocapacitive material resulting in a strong double-layer capacitance in CV scans. We conducted the CV scans in a potential range of -0.224 and 0.824 V (vs. Ag/AgCl) at a scan rate of 50 mV s^{-1} and the electrolyte was 0.1 M aqueous $HClO_4$ solution with oxygen purged. Fig. 7 displays the CV profiles of PdRu/C, Pd_3Ru/C, and Pd_9Ru/C, along with Pd/C and Ru/C for reference purpose (the Pd/C and Ru/C were synthesized from identical processing steps with identical catalyst loading as described in the experimental section). In the CV profile of Pd/C, the Pd oxidation started at ca. 0.75 V and the current became more pronounced around 1 V. During cathodic scan, a notable peak associated with the reduction of PdO was observed at

0.73 V. As the potential was further scanned below 0.3 V, hydrogen adsorption on the Pd surface and hydrogen dissolution in the Pd lattice were occurring [51]. Among our samples, we recorded stronger double-layer capacitances (between 0.3 and 0.55 V) as compared to that of Pd/C, and the magnitude of the double-layer capacitance was increased with increasing Ru amount in the Pd_xRu nanoparticles. Apparently, the Ru/C revealed a stronger capacitive current as compared to those of Pd_xRu/C. In addition, it is noted that in our recent study of PtRu nanoparticles, a similar trend was observed in which the capacitive current is proportional to the amount of Ru atoms on the PtRu surface [52]. This behavior substantiates our rationalization that the Pd_xRu nanoparticles were surface enriched with Ru atoms.

The ORR activities in apparent current density from Pd/C, PdRu/C, Pd_3Ru/C, and Pd_9Ru/C are shown in Fig. 8. The apparent current density is based on the geometric area of the rotating disk electrode. According to the literatures, at potential below 0.6 V, the ORR curve is under mass transport control limited by the diffusion of the dissolved oxygen in the electrolyte whereas at potential between 0.8 and 1 V, the ORR response is dominated by the kinetics of electrocatalysts [53]. Hence, a widely accepted method to determine the ORR activity of an electrocatalyst is based on the half-wave potential, which is defined as the potential at which the magnitude of the current is half of the limiting current. In general, a larger half-wave potential is

indicative of greater ORR activity. Among our samples, the Pd_9Ru/C revealed the best ORR activity and the PdRu/C showed the worse ORR activity. Therefore, the Pd_9Ru/C was chosen as the core for subsequent Cu upd and displacement reaction to fabricate $Pd_9Ru@Pt/C$ for ORR evaluation.

Fig. 9 provides the ORR activities in apparent current density for Pd_9Ru/C, $Pd_9Ru@Pt/C$, and Pt/C. The apparent current density is based on the geometric area of the rotating disk electrode. It is noted that the diffusion-limiting current for these samples at a rotation speed of 1,600 rpm was close to 6 mA cm^{-2}, a value that agreed well with what were observed in earlier literatures [54, 55]. This consistence indicated that our ORR experiments were carried out properly. From Fig. 9, the ORR activities followed the sequence of $Pd_9Ru@Pt/C$ > Pt/C > Pd_9Ru/C. In order to obtain the specific activity of $Pd_9Ru@Pt/C$ and Pt/C, we determined their electrochemical active surface area (ECSA) by imposing CV scans between -0.226 and 0.824 V (vs. RHE) at 50 mV s^{-1} in a deaerated 0.1 M aqueous $HClO_4$ solution. The coulombic charge associated with the hydrogen underpotential deposition region, ranging from ca. 0.05 to 0.35 V (vs. RHE), was divided by 210 μC cm_{Pt}^{-2} to determine the ECSA values. The resulting CV profiles are shown in Fig. 10, and the ECSA value for the $Pd_9Ru@Pt/C$ and Pt/C was 3.1 and 2.9 cm^2, respectively.

Fig. 11 provides the comparison in specific activity and mass activity for oxygen

reduction reaction from Pd_9Ru@Pt/C and Pt/C. The current value was obtained at 0.9 V (vs. RHE) from Fig. 9 and the ECSA area was estimated from Fig. 10. The specific activity of Pd_9Ru@Pt/C and Pt/C was 0.26 and 0.22 (mA cm^{-2}), respectively. In our Pd_9Ru@Pt case, the mechanisms responsible for the enhanced ORR activity are likely to be the lattice strain/ligand effects. In earlier literatures, the interaction between the Pt monolayer and the underlying substrate renders a shift in the *d*-band center that affects the catalytic activity of the surface Pt atoms [56-59]. In addition, it was reported that the Pt atom (1.39 Å) deposited on a Pd (1.37 Å) substrate experiences a minor compressive strain which results in a greater ORR activity [60]. This suggests that the Pd is a promising material serving at the core. In our study, we alloyed the Pd with a small amount of Ru to form Pd_9Ru nanoparticles. Since the atomic radius of the Ru atom is 1.34 Å, we expect to contract the Pd lattice slightly. Our results indicate that the effect of this slight contraction (Pd_9Ru) engenders an improved ORR activity than that of unaltered Pd. Another factor that needs to be considered is the ligand effect in which the Ru atom favors the adsorption of OH on the Pt site [61].

An additional benefit of alloying the Pd with Ru is the reduction in raw material cost as the price for Ru is 41% to that of Pd. (Ru: $186.45/ounce; Pd: $457.51/ounce basing on the average price between 2004 to 2014). Considering the total mass of Pd, Ru, and Pt, the mass activity for Pd_9Ru@Pt/C and Pt/C was identical at 0.107 mA μg^{-1}.

However, if only the mass of Pt was accounted for, the Pd_9Ru@Pt/C exhibited a greater activity (0.38 mA μg^{-1}_{Pt}), as compared to that of Pt/C (0.107 mA μg^{-1}_{Pt}). This is anticipated owing to the reduced mass consumption in Pt monolayer. It is noted that in earlier literatures, Sasaki et al. reported the synthesis of Pt monolayer on Pd nanoparticles with a mass activity of 0.3 mA μg^{-1}_{Pt} [24], and Yang et al. reported the synthesis of Pt monolayer on Ru nanoparticles with a mass activity below 0.3 mA μg^{-1}_{Pt} [62]. Clearly, our results indicated that the Pd_9Ru was able to serve as a desirable core material to support a monolayered Pt for enhanced ORR activities. Since both Pd and Ru are less expensive than that of Pt, our core-shell Pd_9Ru@Pt nanoparticles represent a substantial reduction in Pt consumption and corresponding raw material cost.

To extract the kinetic information, we employed the Koutecky—Levich equation listed below,

$$1/i = 1/i_{kinetic} + 1/i_{diffusion\ limit} = 1/i_{kinetic} + 1/0.62nFAD_{O2}^{2/3}\omega^{1/2}v^{-1/6}C_{O2} \qquad (1)$$

where the i is the experimentally-measured current, the $i_{diffusion\ limit}$ is the diffusion limiting current due to the limitation of mass transport of dissolved oxygen in the 0.1 M aqueous $HClO_4$ solution, the $i_{kinetic}$ is the kinetic current assoicated with the ORR activity, the n is the number of electron transferred in the ORR process, the F is the Faraday constant, the A is the reaction area of the RDE (0.196 cm^2), the D_{O2} is the

diffusivity of dissolved oxygen in the 0.1 M aqueous $HClO_4$ solution (1.93×10^{-5} cm^2 s^{-1}), the ω is the rotation speed of the RDE, the v is the kinematic viscosity of the 0.1 M aqueous $HClO_4$ solution (1.009×10^{-2} cm^2 s^{-1}), and the C_{O2} is the concentration of dissolved oxygen in the 0.1 M aqueous $HClO_4$ solution (1.26×10^{-3} mol L^{-1}). Fig. 12 (a) displays the ORR curves of Pd_9Ru@Pt/C at various rotation speeds of RDE. Among these curves, the ORR curves at voltage below 0.6 V were stabilized at the limiting currents whose values were proportional to the rotation speed as expected from Eq (1). Fig. 12(b) exhibits the Koutecky-Levich plots at different potentials. These curves displayed a consistent pattern with an average slope of 10.88 mA^{-1} $s^{-1/2}$. Accordingly, the electron transfer number, n, was close 4, confirming that the Pd_9Ru@Pt/C nanoparticles proceed the ORR process via a 4-electron route. It is noted that according to the literatures, the Pd, Ru, and Pt catalyzed the ORR via a 4-electron route [63-65].

4. Conclusions

We fabricated Pd_xRu/C using a wet chemical reflux process, and evaluated their ORR activities in an acidic electrolyte. X-ray diffraction patterns of Pd_xRu/C suggested succesful formation of alloy, and the presence of individual Pd and Ru nanoparticles was negligible. Images from transmission electron microscope

confirmed nanoparticles with average size below 3 nm. X-ray absorption spectroscopy (XANES and EXAFS) profiles indicated that the as-synthesized nanoparticles were surface enriched with Ru atoms. Among these samples, the Pd_9Ru/C revealed the strongest ORR activity. To prepare core-shell nanoparticles, the Pd_9Ru/C was subjected to a Cu upd, followed by a galvanic displacement reaction to deposit a Pt monolayer on the Pd_9Ru surface ($Pd_9Ru@Pt$). The $Pd_9Ru@Pt$ demonstrated an even better ORR performance than that of Pt, reaching a mass activity of 0.38 mA μg^{-1}_{Pt}, as compared to that of commercially available Pt nanoparticles (0.107 mA μg^{-1}_{Pt}). From Koutecky—Levich equation, the number of electron transfer for the ORR on the $Pd_9Ru@Pt$ was 4. The ORR enhancement from the $Pd_9Ru@Pt$ is attributed to the strain/ligand effect with additional benefit of the reduction in Pt consumption.

Acknowledgements

Financial supports from Ministry of Science and Engineering (NSC100-2221-E009-075-MY3; 103-2221-E-009-034-MY3) and National Synchrotron Radiation Research Center are greatly appreciated.

References

[1] S. Kawatsu, Journal of Power Sources, 71 (1998) 150-155.

[2] L. Carrette, K.A. Friedrich, U. Stimming, ChemPhysChem, 1 (2000) 162-193.

[3] J. Zhang, PEM fuel cell electrocatalysts and catalyst layers: Fundamentals and Applications, Springer, 2008.

[4] F. Jaouen, E. Proietti, M. Lefèvre, R. Chenitz, J.-P. Dodelet, G. Wu, H.T. Chung, C.M. Johnston, P. Zelenay, Energy & Environmental Science, 4 (2011) 114-130.

[5] P. Costamagna, S. Srinivasan, Journal of Power Sources, 102 (2001) 242-252.

[6] V. Mehta, J.S. Cooper, Journal of Power Sources, 114 (2003) 32-53.

[7] S. Srinivasan, Fuel cells: From Fundamentals to Applications, Springer, 2006.

[8] J. Chen, B. Lim, E.P. Lee, Y. Xia, Nano Today, 4 (2009) 81-95.

[9] J.X. Wang, C. Ma, Y. Choi, D. Su, Y. Zhu, P. Liu, R. Si, M.B. Vukmirovic, Y. Zhang, R.R. Adzic, Journal of the American Chemical Society, 133 (2011) 13551-13557.

[10] K. Joon, Journal of Power Sources, 71 (1998) 12-18.

[11] S.G. Chalk, J.F. Miller, F.W. Wagner, Journal of Power Sources, 86 (2000) 40-51.

[12] T. Toda, H. Igarashi, M. Watanabe, Journal of Electroanalytical Chemistry, 460 (1999) 258-262.

[13] S. Koh, C. Yu, P. Mani, R. Srivastava, P. Strasser, Journal of Power Sources, 172 (2007) 50-56.

[14] D. Wang, H.L. Xin, R. Hovden, H. Wang, Y. Yu, D.A. Muller, F.J. DiSalvo, H.D. Abruña, Nature Materials, 12 (2013) 81-87.

[15] M. Wang, W. Zhang, J. Wang, A. Minett, V. Lo, H. Liu, J. Chen, Journal of Materials Chemistry A, 1 (2013) 2391-2394.

[16] C. Cui, L. Gan, M. Heggen, S. Rudi, P. Strasser, Nature Materials, 12 (2013) 765-771.

[17] V.R. Stamenkovic, B. Fowler, B.S. Mun, G. Wang, P.N. Ross, C.A. Lucas, N.M. Marković, Science, 315 (2007) 493-497.

[18] B.N. Wanjala, B. Fang, S. Shan, V. Petkov, P. Zhu, R. Loukrakpam, Y. Chen, J. Luo, J. Yin, L. Yang, Chemistry of Materials, 24 (2012) 4283-4293.

[19] S.J. Hwang, S.J. Yoo, S. Jang, T.-H. Lim, S.A. Hong, S.-K. Kim, The Journal of Physical Chemistry C, 115 (2011) 2483-2488.

[20] P. Mani, R. Srivastava, P. Strasser, The Journal of Physical Chemistry C, 112 (2008) 2770-2778.

[21] J.X. Wang, H. Inada, L. Wu, Y. Zhu, Y. Choi, P. Liu, W.-P. Zhou, R.R. Adzic, Journal of The American Chemical Society, 131 (2009) 17298-17302.

[22] J.-H. Jang, J. Kim, Y.-H. Lee, I.Y. Kim, M.-H. Park, C.-W. Yang, S.-J. Hwang, Y.-U. Kwon, Energy and Environmental Science, 4 (2011) 4947-4953.

[23] D. Wang, H.L. Xin, Y. Yu, H. Wang, E. Rus, D.A. Muller, H.D. Abruña, Journal

of The American Chemical Society, 132 (2010) 17664-17666.

[24] K. Sasaki, H. Naohara, Y. Cai, Y.M. Choi, P. Liu, M.B. Vukmirovic, J.X. Wang, R.R. Adzic, Angewandte Chemie International Edition, 49 (2010) 8602-8607.

[25] K. Neyerlin, R. Srivastava, C. Yu, P. Strasser, Journal of Power Sources, 186 (2009) 261-267.

[26] P. Strasser, S. Koh, T. Anniyev, J. Greeley, K. More, C. Yu, Z. Liu, S. Kaya, D. Nordlund, H. Ogasawara, Nature Chemistry, 2 (2010) 454-460.

[27] P. Mani, R. Srivastava, P. Strasser, Journal of Power Sources, 196 (2011) 666-673.

[28] Y.-J. Lee, Y.-C. Hsieh, H.-C. Tsai, I. Lu, Y.-H. Wu, T.H. Yu, J.-F. Lee, B.V. Merinov, W.A. Goddard III, P.-W. Wu, Applied Catalysis B: Environmental, 150-151 (2014) 636-646.

[29] F.J. Lai, W.N. Su, L.S. Sarma, D.G. Liu, C.A. Hsieh, J.F. Lee, B.J. Hwang, Chemistry-A European Journal, 16 (2010) 4602-4611.

[30] I. Spanos, J.J. Kirkensgaard, K. Mortensen, M. Arenz, Journal of Power Sources, 245 (2014) 908-914.

[31] F. Tao, M.E. Grass, Y. Zhang, D.R. Butcher, J.R. Renzas, Z. Liu, J.Y. Chung, B.S. Mun, M. Salmeron, G.A. Somorjai, Science, 322 (2008) 932-934.

[32] S.L. Knupp, M.B. Vukmirovic, P. Haldar, J.A. Herron, M. Mavrikakis, R.R.

Adzic, Electrocatalysis, 1 (2010) 213-223.

[33] L. Hou, H. Qiu, Journal of Power Sources, 216 (2012) 28-32.

[34] K. Sasaki, H. Naohara, Y. Choi, Y. Cai, W.-F. Chen, P. Liu, R.R. Adzic, Nature Communications, 3 (2012) 1115.

[35] K.A. Kuttiyiel, K. Sasaki, D. Su, M.B. Vukmirovic, N.S. Marinkovic, R.R. Adzic, Electrochimica Acta, 110 (2013) 267-272.

[36] M. Shao, K. Shoemaker, A. Peles, K. Kaneko, L. Protsailo, Journal of The American Chemical Society, 132 (2010) 9253-9255.

[37] J. Greeley, J.K. Nørskov, M. Mavrikakis, Annual Review of Physical Chemistry, 53 (2002) 319-348.

[38] J. Greeley, M. Mavrikakis, Nature Materials, 3 (2004) 810-815.

[39] J. Kitchin, J.K. Nørskov, M. Barteau, J. Chen, Journal of Chemical Physics, 120 (2004) 10240-10246.

[40] A.U. Nilekar, Y. Xu, J. Zhang, M.B. Vukmirovic, K. Sasaki, R.R. Adzic, M. Mavrikakis, Topics in Catalysis, 46 (2007) 276-284.

[41] J. Zhang, M.B. Vukmirovic, K. Sasaki, A.U. Nilekar, M. Mavrikakis, R.R. Adzic, Journal of The American Chemical Society, 127 (2005) 12480-12481.

[42] L. Ma, H. He, A. Hsu, R. Chen, Journal of Power Sources, 241 (2013) 696-702.

[43] J. Fisher, N. Cabello-Moreno, E. Christian, D. Thompsett, Electrochemical and

Solid-State Letters, 12 (2009) B77-B81.

[44] D. Wu, Z. Zheng, S. Gao, M. Cao, R. Cao, Physical Chemistry Chemical Physics, 14 (2012) 8051-8057.

[45] Y.-C. Hsieh, L.-C. Chang, P.-W. Wu, Y.-M. Chang, J.-F. Lee, Applied Catalysis B: Environmental, 103 (2011) 116-127.

[46] S. Tripathi, S. Bharadwaj, S. Dharwadkar, Journal of Phase Equilibria, 14 (1993) 638-642.

[47] Y. Sugawara, A. Yadav, A. Nishikata, T. Tsuru, Journal of the Electrochemical Society, 155 (2008) B897-B902.

[48] D.G. Liu, J.F. Lee, M.T. Tang, J. Molecular Catalysis A: Chemical, 240 (2005) 197-202

[49] G.H. Via, J.H. Sinfelt, G. Meitzner, F.W. Lytle, Mater. Res. Soc. Symp. Proc., 143 (1988) 111.

[50] J. Sinfelt, Journal of Catalysis, 29 (1973) 308-315.

[51] M. Grdeń, M. Łukaszewski, G. Jerkiewicz, A. Czerwiński, Electrochimica Acta, 53 (2008) 7583-7598.

[52] C.W. Kuo, I.T. Lu, L.C. Chang, Y.C. Hsieh, Y.C. Tseng, P.W. Wu, J.F. Lee, J. Power Sources, 240 (2013) 122-130.

[53] U. Paulus, T. Schmidt, H. Gasteiger, R. Behm, Journal of Electroanalytical

Chemistry, 495 (2001) 134-145.

[54] V. Stamenkovic, T. Schmidt, P. Ross, N. Markovic, The Journal of Physical Chemistry B, 106 (2002) 11970-11979.

[55] H.A. Gasteiger, S.S. Kocha, B. Sompalli, F.T. Wagner, Applied Catalysis B: Environmental, 56 (2005) 9-35.

[56] B. Hammer, J.K. Nørskov, Advances in Catalysis, 45 (2000) 71-129.

[57] J. Zhang, M.B. Vukmirovic, Y. Xu, M. Mavrikakis, R.R. Adzic, Angewandte Chemie International Edition, 44 (2005) 2132-2135.

[58] A.U. Nilekar, Y. Xu, J. Zhang, M.B. Vukmirovic, K. Sasaki, R.R. Adzic, M. Mavrikakis, Topics in Catalysis, 46 (2007) 276-284.

[59] J.X. Wang, H. Inada, L. Wu, Y. Zhu, Y. Choi, P. Liu, W.-P. Zhou, R.R. Adzic, J. American Chemical Society, 131 (2009) 17298-17302.

[60] R.R. Adzic, J. Zhang, K. Sasaki, M.B. Vukmirovic, M. Shao, J. Wang, A.U. Nilekar, M. Mavrikakis, J. Valerio, F. Uribe, Topics in Catalysis, 46 (2007) 249-262.

[61] J. Zhang, M.B. Vukmirovic, K. Sasaki, A.U. Nilekar, M. Mavrikakis, R.R. Adzic, J. American Chemical Society, 127 (2005) 12480-12481.

[62] L. Yang, M.B. Vukmirovic, D. Su, K. Sasaki, J.A. Herron, M. Mavrikakis, S. Liao, R.R. Adzic, The Journal of Physical Chemistry C, 117 (2013) 1748-1753.

[63] J. Salvador-Pascual, S. Citalán-Cigarroa, O. Solorza-Feria, Journal of Power

Sources, 172 (2007) 229-234.

[64] N.M. Marković, P.N. Ross, Journal of The Electrochemical Society, 141 (1994) 2590-2597.

[65] N.M. Markovic, H.A. Gasteiger, P.N. Ross Jr, The Journal of Physical Chemistry, 99 (1995) 3411-3415.

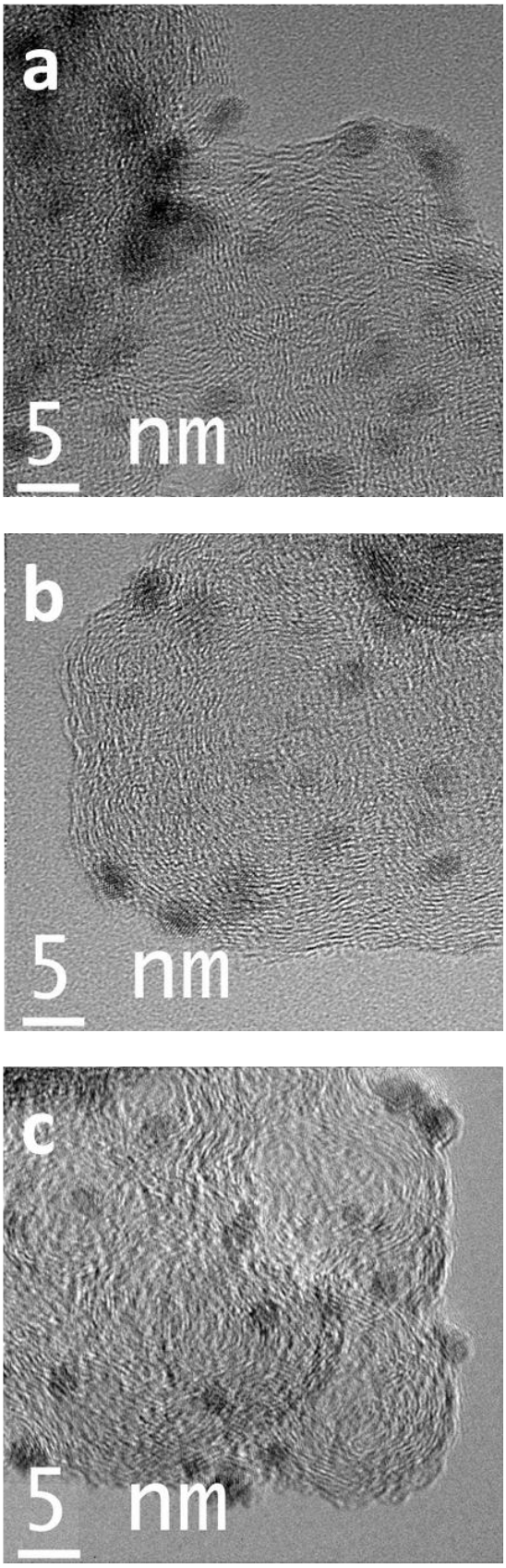

Fig. 1. The representative TEM images of (a) PdRu/C, (b) Pd_3Ru/C, and (c) Pd_9Ru/C.

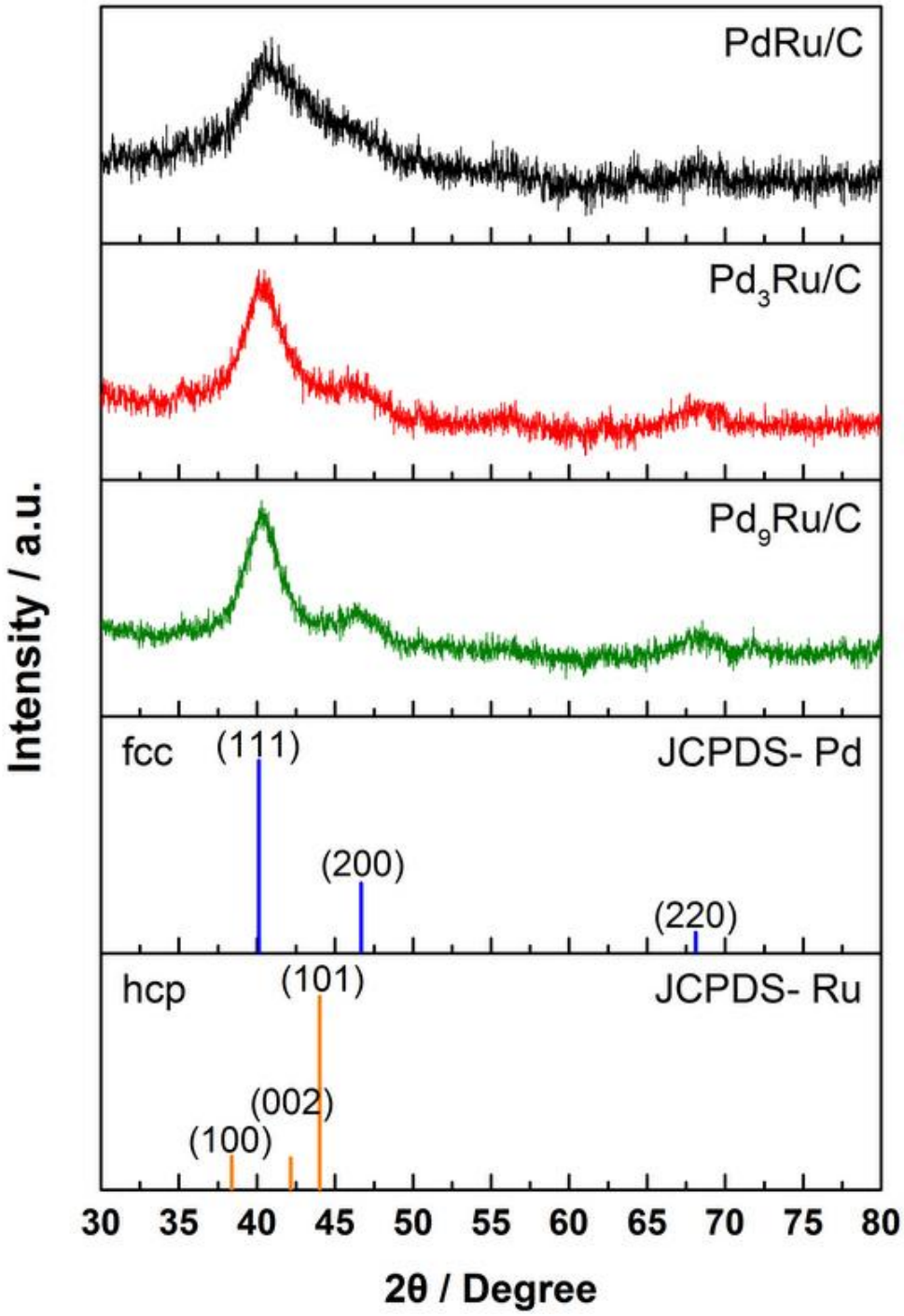

Fig. 2. The XRD patterns of PdRu/C, Pd_3Ru/C, and Pd_9Ru/C, as well as fcc Pd (JCPDS: no. 88-2335) and hcp Ru (JCPDS: no. 06-0663).

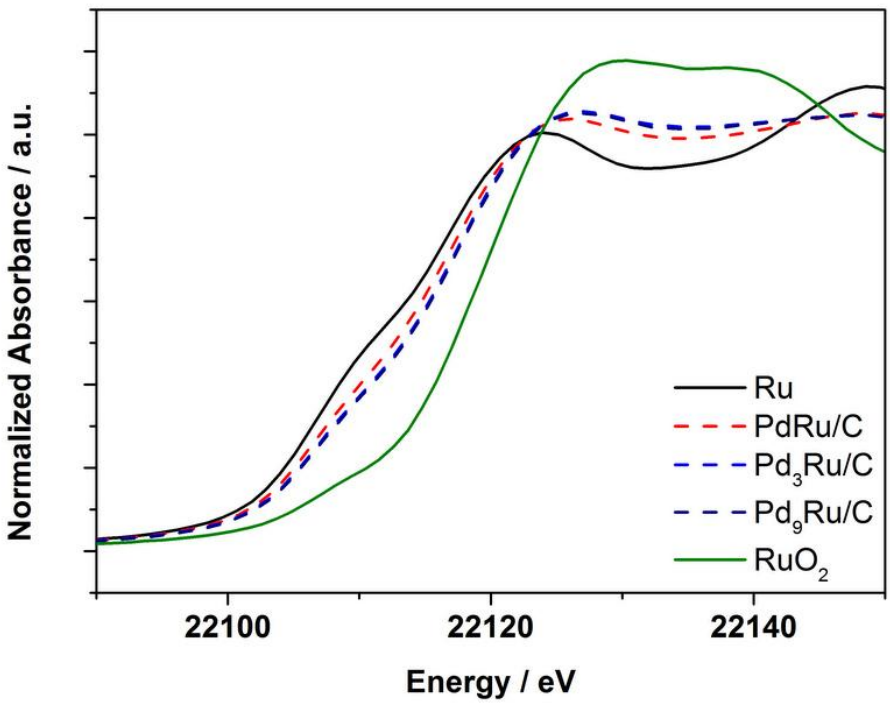

Fig. 3. The Ru K-edge XANES spectra of PdRu/C, Pd_3Ru/C, Pd_9Ru/C, Ru, and RuO_2.

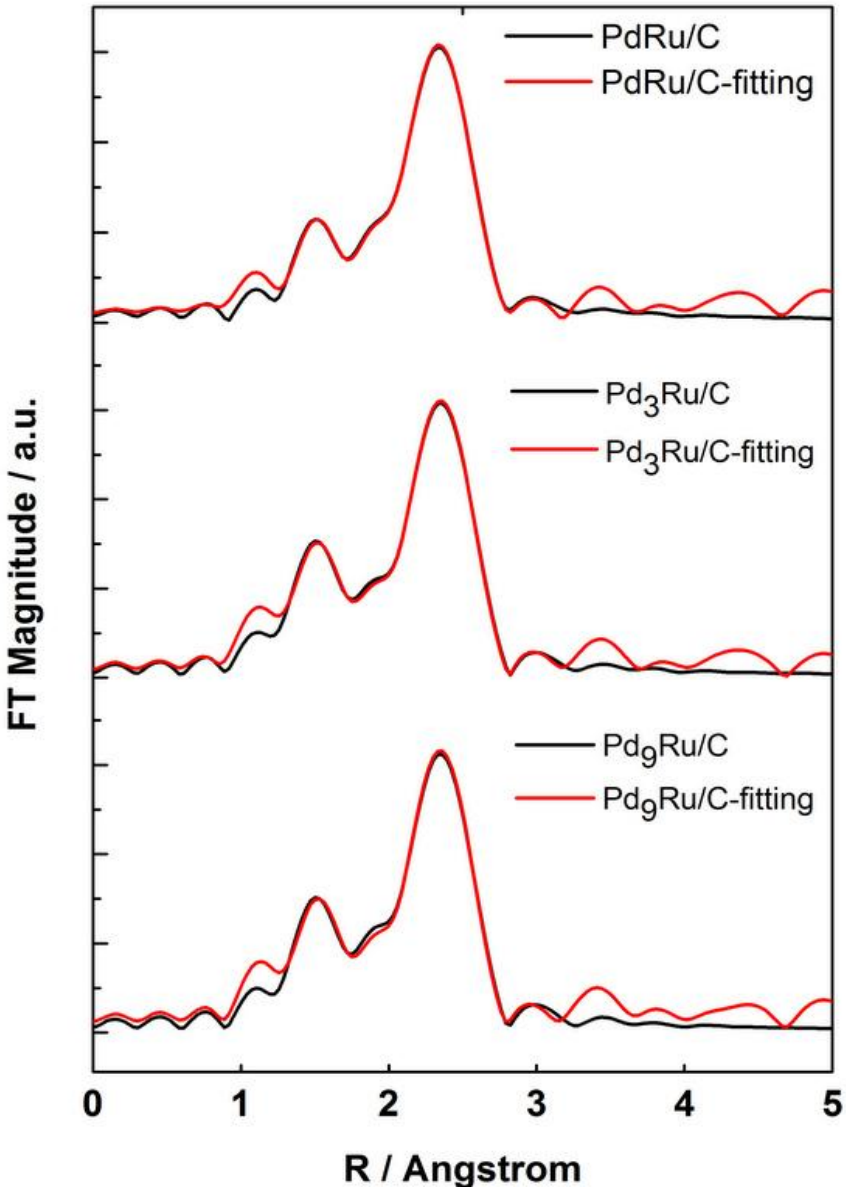

Fig. 4. The Ru K-edge Fourier-transformed EXAFS spectra and their respective fitting results for PdRu/C, Pd_3Ru/C, and Pd_9Ru/C from Fig. 3.

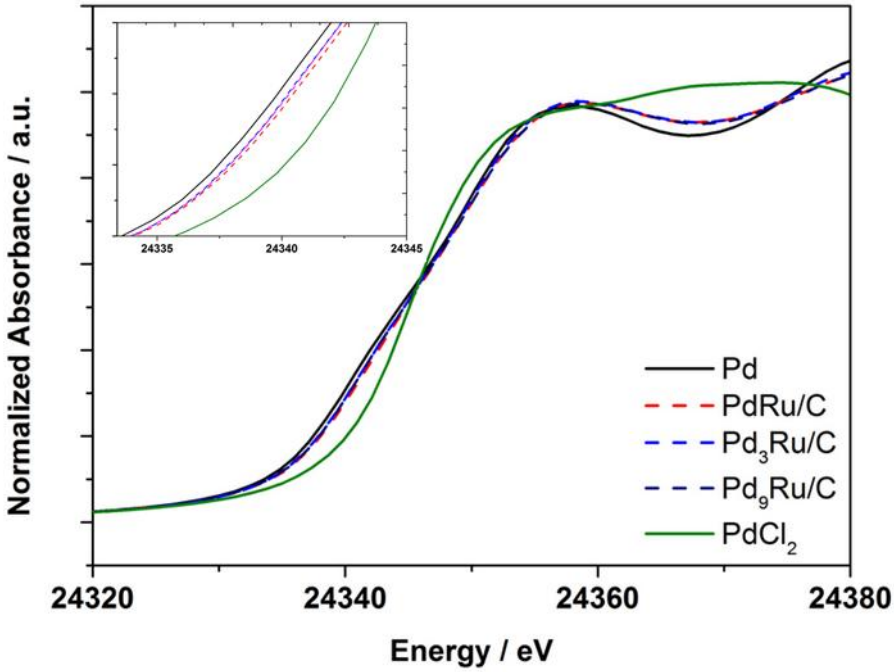

Fig. 5. The Pd K-edge XANES spectra of PdRu/C, Pd_3Ru/C, Pd_9Ru/C, Pd, and $PdCl_2$.

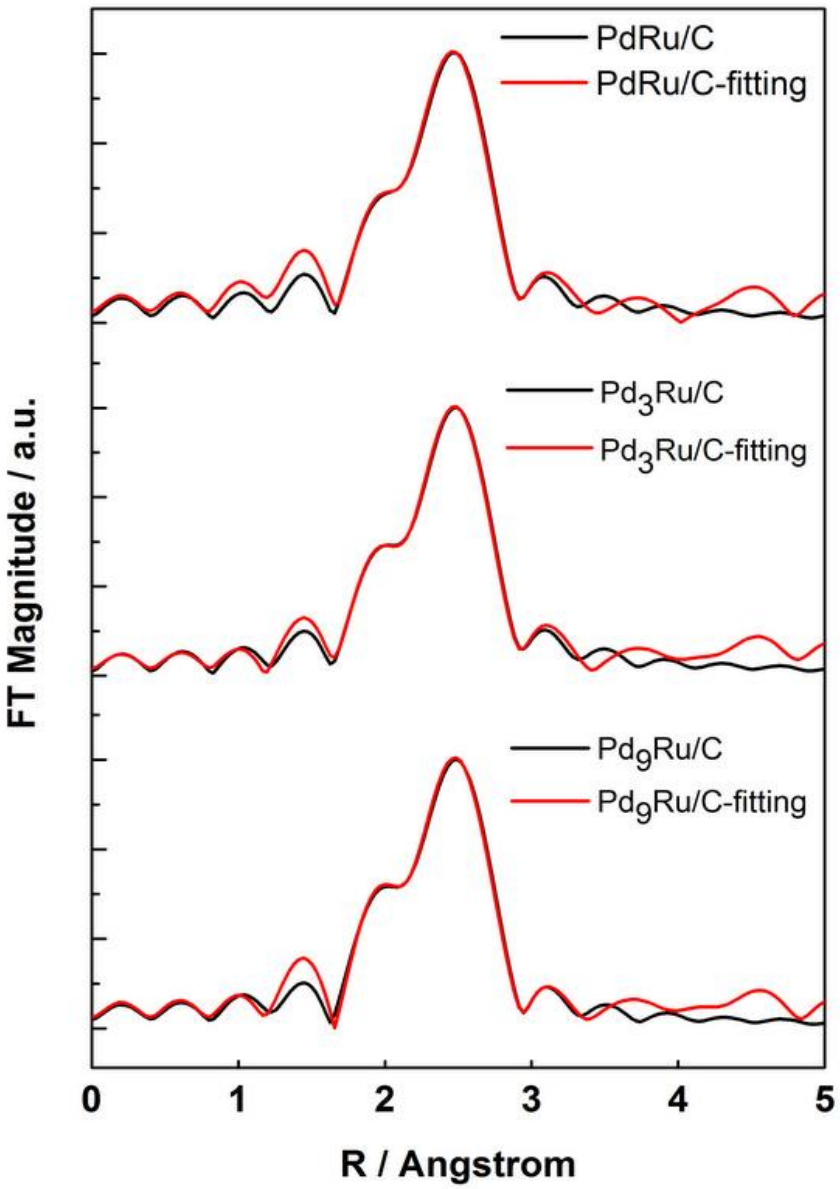

Fig. 6. The Pd K-edge EXAFS Fourier-transformed EXAFS spectra and their respective fitting results for PdRu/C, Pd_3Ru/C, and Pd_9Ru/C from Fig. 5.

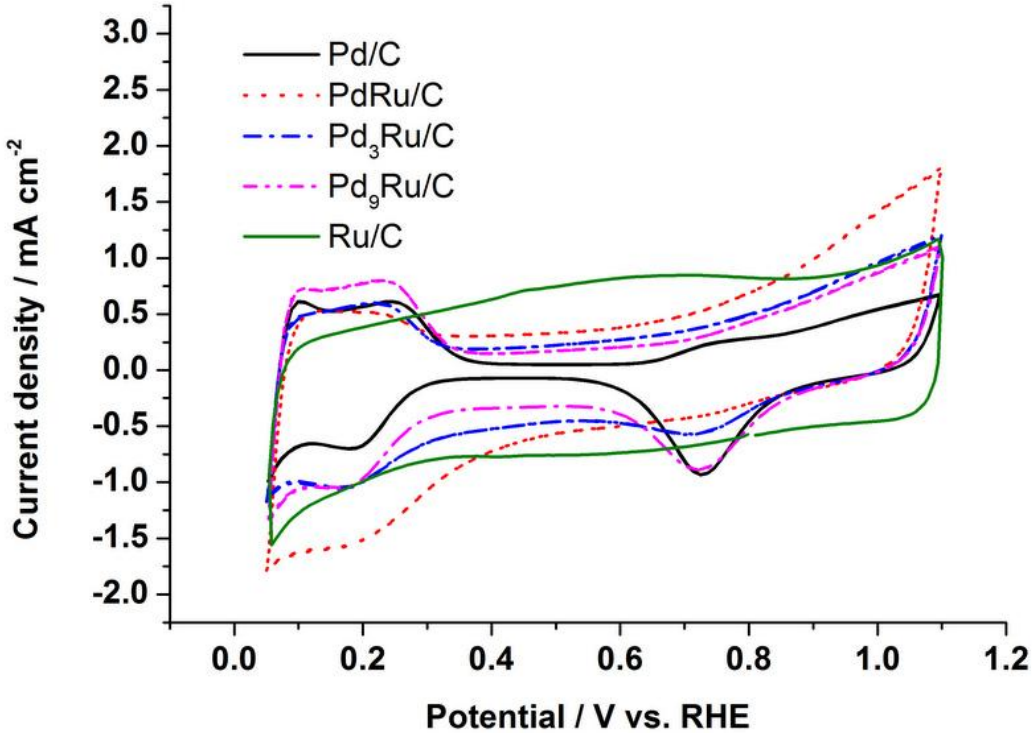

Fig. 7. The CV profiles of PdRu/C, Pd_3Ru/C, Pd_9Ru/C, Ru/C, and Pd/C in deaerated 0.1 M $HClO_4$ aqueous solution at a scan rate of 50 mV s^{-1}.

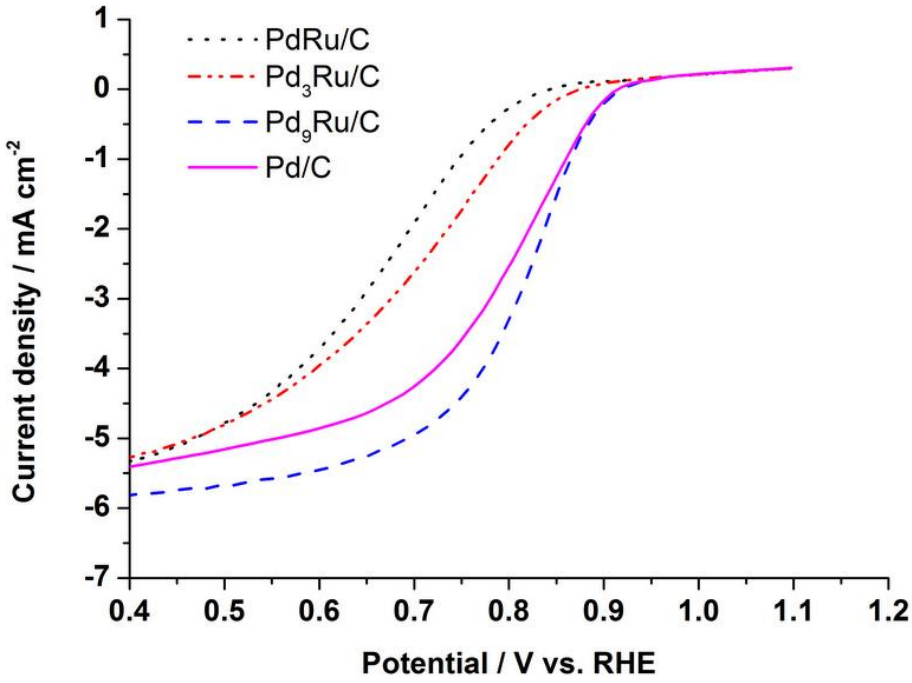

Fig. 8. The ORR activities in apparent current density for PdRu/C, Pd_3Ru/C, and Pd_9Ru/C. The experiments were conducted in an oxygen-saturated 0.1 M $HClO_4$ aqueous solution at 1,600 rpm and a scan rate of 10 mV s^{-1}. The apparent current density is based on the geometric area of the rotating disk electrode.

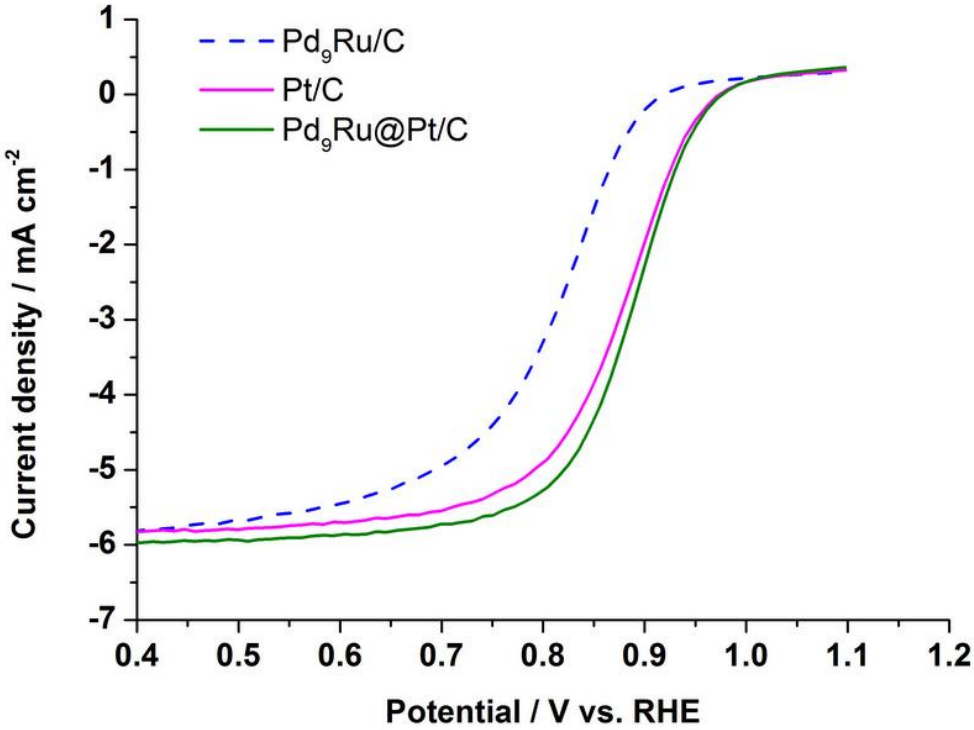

Fig. 9. The ORR activities in apparent current density for Pd_9Ru/C, $Pd_9Ru@Pt/C$, and Pt/C. The experiments were conducted in an oxygen-saturated 0.1 M $HClO_4$ aqueous solution at 1,600 rpm and a scan rate of 10 mV s^{-1}. The apparent current density is based on the geometric area of the rotating disk electrode.

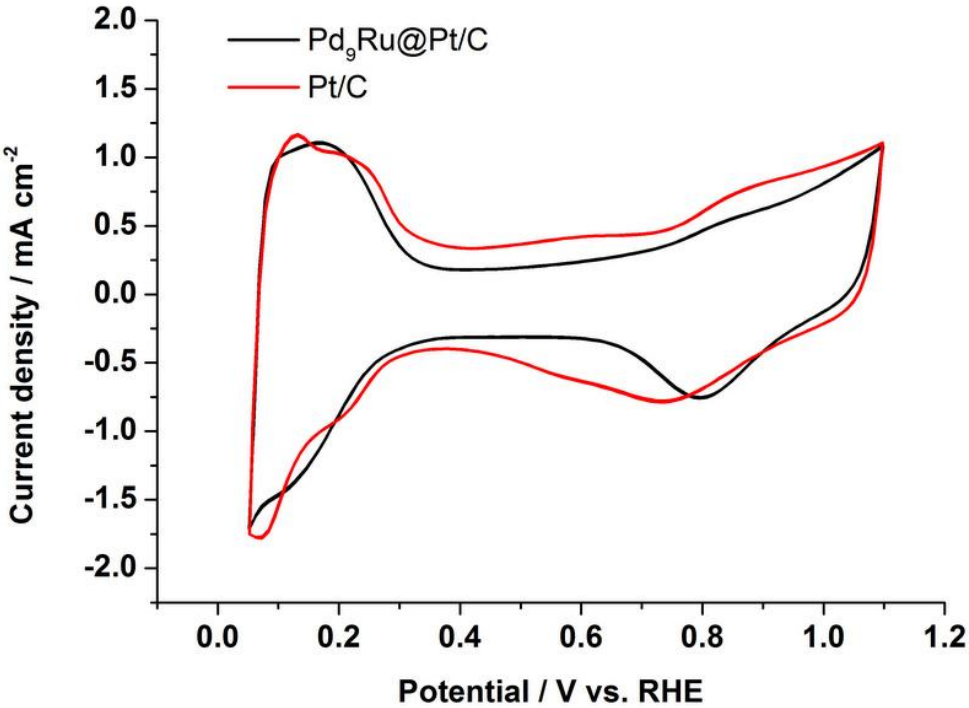

Fig. 10. The CV profiles of Pd_9Ru@Pt/C and Pt/C in deaerated 0.1 M $HClO_4$ aqueous solution at a scan rate of 50 mV s^{-1}.

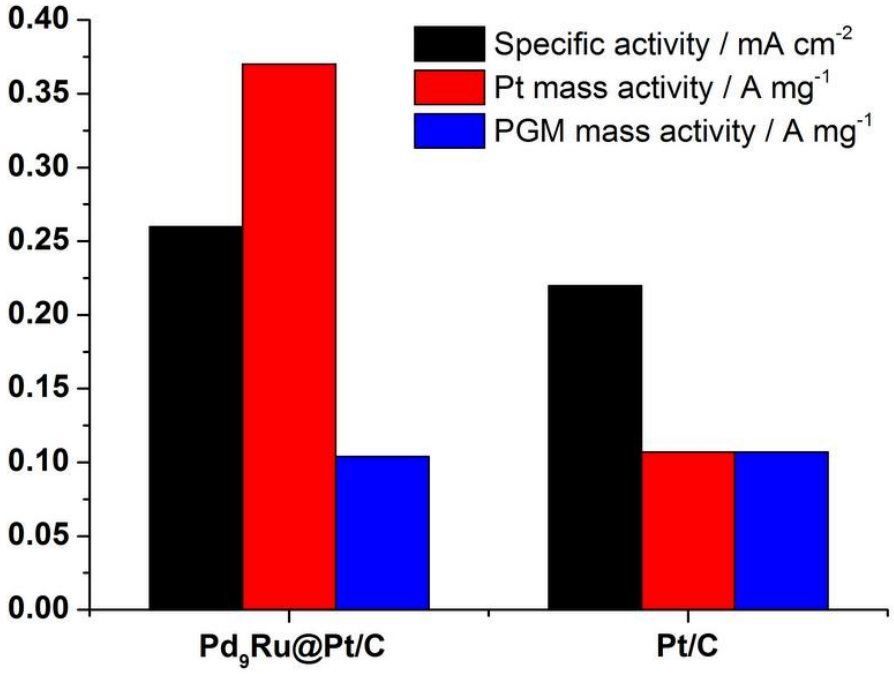

Fig. 11. Comparison in the specific activity and mass activity for oxygen reduction reaction from Pd_9Ru@Pt/C and Pt/C. The current value is determined at 0.9 V (vs. RHE) from Fig. 9 and the electrochemical active surface area is estimated from Fig. 10.

(a)

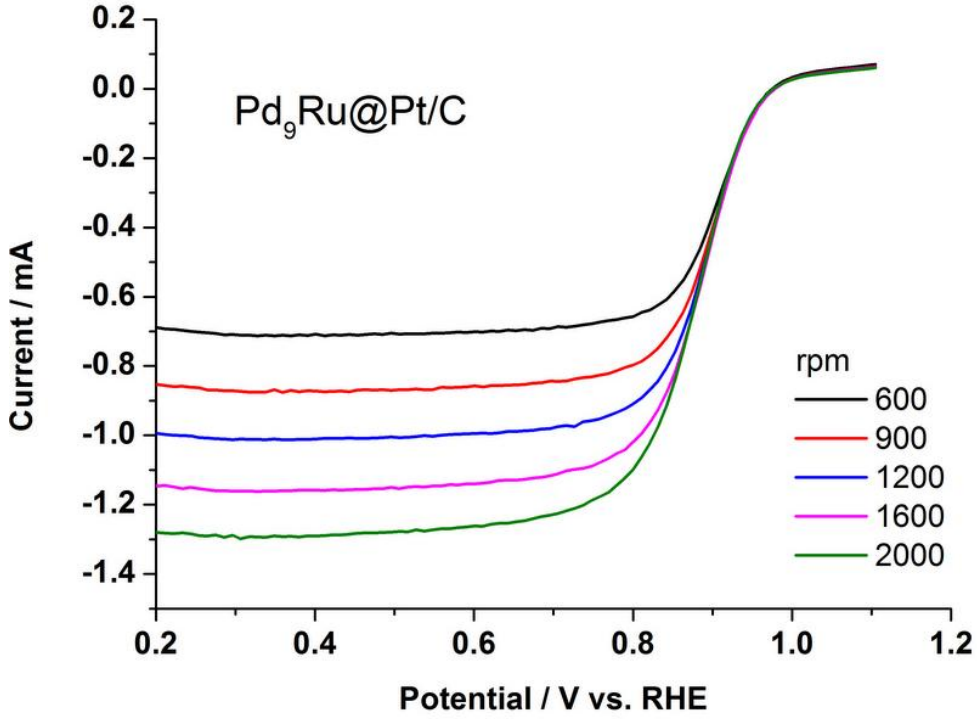

(b)

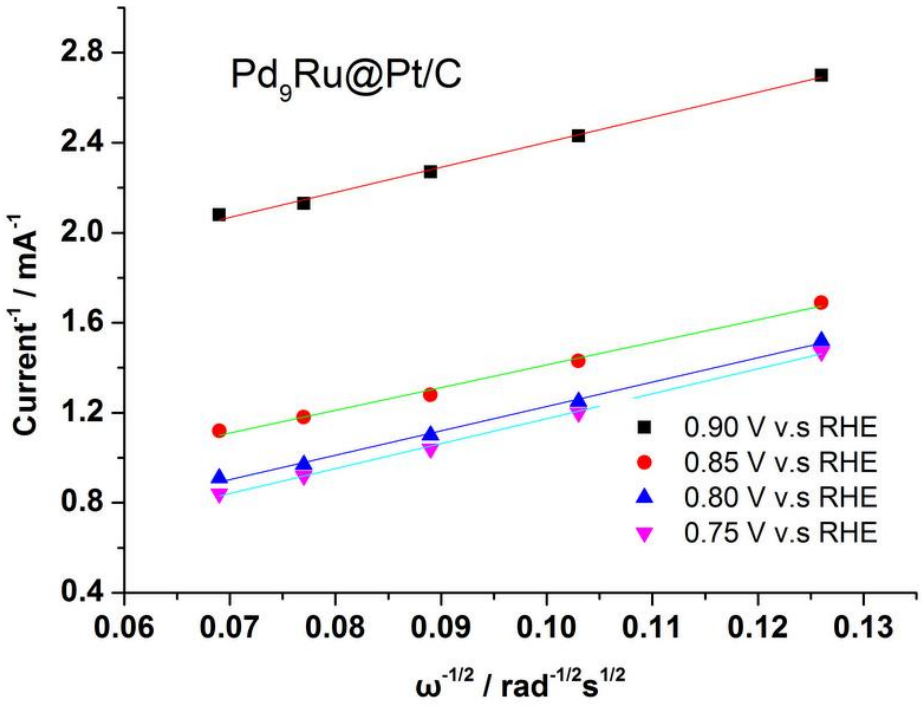

Fig. 12. (a) RDE measurements of the ORR curves from Pd_9Ru@Pt/C at various rotation speeds. (b) the Koutecky-Levich plot at different voltages.

Table 1. EXAFS fitting parameters at the Ru K-edge for PdRu/C, Pd_3Ru/C, and Pd_9Ru/C, respectively.

	Path	Coordination number, N	Bond distance, R (Å)	Inner potential shift, ΔE_0 (eV)	Debye-Waller factor, $\Delta\sigma_j^2$ ($*10^{-3}$ Å^2)
PdRu/C	Ru-O	1.35	2.02	-0.09	6.82
	Ru-Ru	4.34	2.65	-9.89	7.58
	Ru-Pd	0.72	2.76	5.74	7.08
Pd_3Ru/C	Ru-O	1.76	2.01	-0.81	7.61
	Ru-Ru	4.07	2.66	-8.90	8.41
	Ru-Pd	0.82	2.77	7.07	9.78
Pd_9Ru/C	Ru-O	1.67	2.02	-0.05	7.33
	Ru-Ru	3.93	2.66	-8.56	7.60
	Ru-Pd	0.70	2.82	10.16	7.98

Table 2. EXAFS fitting parameters at the Pd K-edge for PdRu/C, Pd_3Ru/C, and Pd_9Ru/C, respectively.

	Path	Coordination number, N	Bond distance, R (Å)	Inner potential shift, ΔE_0 (eV)	Debye-Waller factor, $\Delta\sigma_j^2$ ($*10^{-3}$ Å^2)
PdRu/C	Pd-Pd	6.2	2.68	-6.77	8.57
	Pd-Ru	1.9	2.75	-13.68	3.18
Pd_3Ru/C	Pd-Pd	7.2	2.69	-8.45	6.67
	Pd-Ru	1.8	2.77	-19.61	1.63
Pd_9Ru/C	Pd-Pd	6.9	2.71	-7.60	5.93
	Pd-Ru	1.7	2.80	-19.90	2.74